

Homotopic Object Reconstruction Using Natural Neighbor Barycentric Coordinates

Ojaswa Sharma¹ and François Anton²

¹ Department of Computer Science and Engineering,
Indian Institute of Technology Bombay,
Mumbai, 400076, India
`ojaswa@cse.iitb.ac.in`

² Department of Informatics and Mathematical Modelling,
Technical University of Denmark, Lyngby, 2800, Denmark
`fa@imm.dtu.dk`

Abstract. One of the challenging problems in computer vision is object reconstruction from cross sections. In this paper, we address the problem of 2D object reconstruction from arbitrary linear cross sections. This problem has not been much discussed in the literature, but holds great importance since it lifts the requirement of order within the cross sections in a reconstruction problem, consequently making the reconstruction problem harder. Our approach to the reconstruction is via continuous deformations of line intersections in the plane. We define Voronoi diagram based barycentric coordinates on the edges of n -sided convex polygons as the area stolen by any point inside a polygon from the Voronoi regions of each open oriented line segment bounding the polygon. These allow us to formulate homotopies on edges of the polygons from which the underlying object can be reconstructed. We provide results of the reconstruction including the necessary derivation of the gradient at polygon edges and the optimal placement of cutting lines. Accuracy of the suggested reconstruction is evaluated by means of various metrics and compared with one of the existing methods.

Keywords: Voronoi diagram, natural neighbor, Homotopy, continuous deformations, reconstruction, linear cross sections.

1 Introduction

Object reconstruction from cross sections is a well known problem. Generally a spatial ordering within the cross sections aids reconstruction. We consider the problem of reconstructing an object from arbitrary linear cross sections. Such cross sectional data can be obtained from many physical devices. An example is an acoustic probe that can obtain range information of an object by sending an acoustic pulse.

The problem of reconstruction from arbitrary cross sections has been studied by [15,9,10]. Sidlesky et al. [15] define sampling conditions on the reconstruction, while in our reconstruction algorithm, we allow the sampling to be sparse.

Methods proposed by Liu et al. [9], and Memari and Boissonnat [10] are both based on Voronoi diagrams. Memari and Boissonnat also provide rigorous proof of their reconstruction. Our approach to reconstruction considers the “presence” or “absence” of information along any intersecting line. This is in contrast to [15], where the authors consider that a line not intersecting the object does not contribute to the reconstruction. In our algorithm, such a line is considered to contribute to the reconstruction by defining a linear section, no part of which belongs to the reconstruction.

Memari and Boissonnat [10] provide a topological reconstruction method utilizing the Delaunay triangulation of the set of segments of intersecting lines. They claim an improvement over the method by Liu et al. [9] by producing reconstructions that are not topologically effected by lines that do not intersect the object under consideration. Their reconstruction boundary, however, is a piecewise linear approximation of the boundary of the original object. In this work, we produce smooth reconstruction of the object via continuous deformations. Therefore, we anticipate better reconstruction accuracy compared to the work by Memari and Boissonnat [10].

This paper is organized as follows. Section 2 defines the reconstruction problem mathematically. We introduce the concept of homotopy continuation in section 3 followed by the main reconstruction algorithm in section 4. We discuss our Voronoi diagram based edge barycentric coordinates on convex polygons here and provide details of our homotopy based reconstruction algorithm. We provide results of the reconstruction in section 5 and analyze the accuracy of our algorithm.

2 Problem Definition

Given a set of lines $\{\mathcal{L}_i : i \in [0, n - 1]\}$ in a plane, intersecting an object \mathcal{O} along segments $\{\mathcal{S}_{i,j} : j \in [0, m_i - 1]\}$, the problem of object reconstruction from arbitrary linear cross sections is to reconstruct an object \mathcal{O} from $\mathcal{S}_{i,j}$ such that the reconstruction \mathcal{R} satisfies

$$\mathcal{L}_i \bigcap \mathcal{O} = \mathcal{L}_i \bigcap \mathcal{R}, \quad (1)$$

and that \mathcal{R} is homeomorphic to \mathcal{O} . Further, the reconstruction should also be geometrically close to the object. We quantify the geometric closeness in our reconstruction by means of several area based ratios such as the ratio of area of reconstruction and the area of the object, and the ratio of the absolute difference of the two areas and the area of the object. Length ratio is also a good indicator of geometric closeness. Furthermore, Hausdorff distance between the two curves gives a good measure of the distance between them.

In this context we impose no restrictions on the ordering or arrangement of the intersecting lines. However, the placement of intersecting lines plays an important role in the correctness of the reconstruction. A placement that covers salient object features results in a better reconstruction. In order to quantify an optimal placement, consider a set of intersecting lines in a plane along with

the object to be reconstructed. The intersecting lines partition the object into smaller regions. Considering the simply connected boundary of the object that belongs to a region (see the highlighted curve segment in Fig. 1(a)), *tortuosity* [6], which gives a simple measure of how twisted a curve is, can be computed. It is defined as the arc-chord ratio of a parametric curve $C = (x(t), y(t))$ on the interval $[t_0, t_1]$ [13]

$$\tau = \frac{L}{C} = \frac{\int_{t_0}^{t_1} \sqrt{x'(t)^2 + y'(t)^2}}{\sqrt{(x(t_1) - x(t_0))^2 + (y(t_1) - y(t_0))^2}}. \quad (2)$$

τ can be considered as a measure of straightness of a curve. According to (2), tortuosity of a circle is infinite [13] since the chord length is zero for $t_1 = t_0$. This definition can be extended for parts of the object boundary that are not intersected by any of the lines (for example, an isolated blob shown in Fig. 1(a)). In such a case, the two end points do not exist and therefore these can be set to a single point (i.e., $t_1 = t_0$) without loss of generality. Therefore, for isolated object parts that have no intersection with the cutting lines, τ is taken as infinity.

It is not difficult to see that higher the value of τ for any region, more it is susceptible to generate part of the reconstruction that is non-homeomorphic to the object. However, if the sampling is such that the intersecting lines are chosen along the medial axis of the object, then such regions can be avoided (see Fig. 1(b)). In that case, τ remains close to one for different regions. Such a sampling is illustrated in subsection 5.1 for deriving accuracy statistics for the proposed reconstruction method.

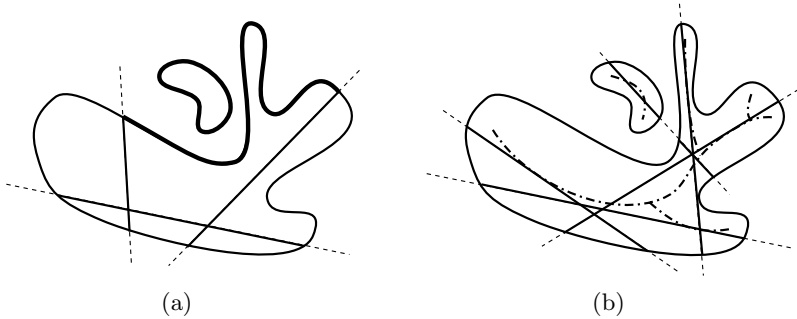


Fig. 1. Sampling condition on the intersecting lines. (a) Under-sampling. (b) Optimal sampling along medial axis.

The skeleton (\mathcal{K}) of the object and the skeleton (\mathcal{K}^c) of the complement of the object in its convex hull provide optimal placement of the cutting lines. Indeed, except if the object is a disc, the intersection of the closure of the union of \mathcal{K} and \mathcal{K}^c with the boundaries of the object correspond to the local extrema of curvature of the boundary object. In addition, the tangent to \mathcal{K} or \mathcal{K}^c at

these points of intersection with the boundaries of the object correspond to the normal to the object boundary at these points in the case of regular points and the axis of the normal cone in the case of singular points (see Fig. 2). In the case of a disc, the curvature is constant, and the skeleton is reduced to a point (its center), while the complement of the disc in its convex hull is the empty space. The notion of using the skeleton of an object for optimal sampling comes from the Geometric Sampling Theorem [14]. As with 1D signals, the sampling must consider the highest frequency present in the signal, for manifolds, sampling must ensure that the regions of high curvature are measured [14]. In our case, we ensure this by sampling along the skeleton. Another desired trait

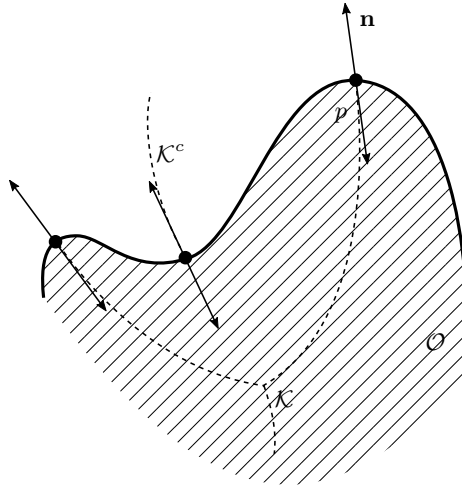


Fig. 2. Optimal placement of cutting lines. \mathcal{O} is the object with \mathcal{K} being its skeleton and \mathcal{K}^c being the skeleton of its complement. The closure of these skeletons touches the boundary of \mathcal{O} at the local extrema points.

of a reconstruction is smoothness, and we will show that the proposed method of continuous deformations results in a reconstruction that is at least C^1 .

3 Homotopy Continuation

Homotopy is concerned with identification of paths between objects that can be continuously deformed into each other. The history of study of homotopy dates back in the late 1920's when the homotopy theory was formalized.

Definition 1. Let $f : X \rightarrow Y$ and $g : X \rightarrow Y$ be two continuous maps between topological spaces X and Y . These maps are called homotopic, $f \simeq g$, if there is a homotopy or a continuous map $\mathcal{H} : X \times [0, 1] \rightarrow Y$ between them, such that $\mathcal{H}(x, 0) = f(x)$ and $\mathcal{H}(x, 1) = g(x)$ for all $x \in X$.

Therefore, we can write the homotopy $\mathcal{H}_\lambda : X \rightarrow Y$ as

$$\mathcal{H}_\lambda(x) = \mathcal{H}(x, \lambda), \quad (3)$$

and thus, $\mathcal{H}_0 = f$ and $\mathcal{H}_1 = g$. One can visualize how the deformation h continuously takes f to g (see Fig. 3) by varying the parameter λ .

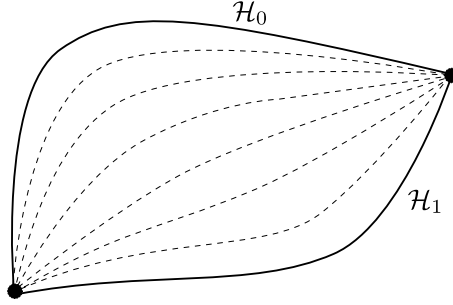


Fig. 3. Continuous deformation

One can impose additional constraints on the deformation path. For example, a specific constraint on fixed endpoints leads to homotopy of paths. For two pairs of homotopic maps $X \xrightarrow{f \simeq g} Y \xrightarrow{\bar{f} \simeq \bar{g}} Z$, the compositions $\bar{f} \circ f$ and $\bar{g} \circ g$ are also homotopic via the composition $\bar{\mathcal{H}}_\lambda \circ \mathcal{H}_\lambda$. Further, for two pairs of homotopic maps $f_i \simeq g_i : X_i \rightarrow Y_i, i = 1, 2$, the maps $f_1 \times f_2$ and $g_1 \times g_2$ from $X_1 \times X_2$ into $Y_1 \times Y_2$ are also homotopic via $\mathcal{H}_\lambda^{(1)} \times \mathcal{H}_\lambda^{(2)}$, in which case it is called a *product homotopy* [7].

Continuous deformations have been successfully used to solve non-linear system of equations that are otherwise hard to solve. A homotopy tries to solve a difficult problem with unknown solutions by starting with a simple problem with known solutions. Stable predictor-corrector and piecewise-linear methods for solving such problems exist (see Allgower and Georg [3]). The system $\mathcal{H}(x, \lambda) = 0$ implicitly defines a curve or 1-manifold of solution points as λ varies in $[0, 1]$ and x is fixed.

Given smooth \mathcal{H} and existence of $u_0 \in \mathbb{R}^{N+1}$ such that $\mathcal{H}(u_0) = 0$ and $\text{rank}(\mathcal{H}'(u_0)) = N$, there exists a smooth curve $c : \alpha \in J \mapsto c(\alpha) \in \mathbb{R}^{N+1}$ for some open interval J containing zero such that for all $\alpha \in J$ (Allgower and Georg [3])

1. $c(0) = u_0$,
2. $\mathcal{H}(c(\alpha)) = 0$,
3. $\text{rank}(\mathcal{H}'(c(\alpha))) = N$,
4. $c'(\alpha) \neq 0$.

In this work, we use homotopy or continuous deformations for object reconstruction. This is discussed in the next section.

4 Reconstruction Algorithm

Starting with a set of cross sections $\{\mathcal{S}_{i,j}\}$ for lines $\{\mathcal{L}_i\}$ in a plane, we restrict reconstruction in the bounding box \mathcal{B}_{box} of the cross sections. The set of lines $\{\mathcal{L}_i\}$ partition \mathcal{B}_{box} into a set of convex polygons $\{\mathcal{G}_k\}, k \in [0, p-1]$. This is shown in Fig. 4 where \mathcal{O} is drawn dotted, the set of lines are shown dashed with the cross sections as thick solid lines, and the boundary of the bounding box is shown dashed. Our reconstruction algorithm consists of assigning a homotopy \mathcal{H}_k to every polygon \mathcal{G}_k . The reconstruction is then obtained as a union of reconstructions within each polygon:

$$\mathcal{R} = \bigcup_k \{(x, y) : \mathcal{H}_k = 0\}. \quad (4)$$

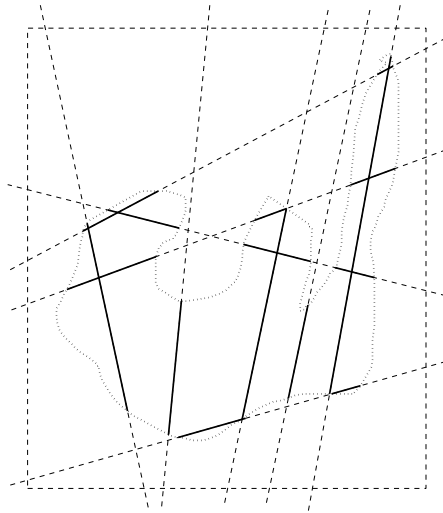


Fig. 4. A set of lines intersecting an object (dotted)

A homotopy can be seen as a smooth transition from one map to another. We can extend this definition to multiple maps by defining a homotopy in multiple variables

$$\mathcal{H}(\lambda_0, \lambda_1, \dots, \lambda_{s-1}) = \sum_{t=0}^{s-1} f_t \lambda_t, \quad (5)$$

with

$$\sum_{t=0}^{s-1} \lambda_t = 1. \quad (6)$$

The homotopy parameters must sum up to unity in order to define the deformation \mathcal{H} inside the convex hull of the domain. In our case, the domain is a polygon formed by straight line segments.

4.1 Edge Maps

Using (5), a smooth map can be defined over \mathcal{G}_k for a choice of maps $\{f_t\}, t \in [0, s_k - 1]$ defined on s_k edges of \mathcal{G}_k . Let these maps be called *edge maps*. For continuity across all polygons, the definition of the edge maps must be consistent. Since, polygon edges are a subset of the cross section lines, it suffices to define edge maps over $\{\mathcal{L}_i\}$.

An edge map f_i should completely describe the boundary, interior and exterior of the intersection of \mathcal{L}_i with \mathcal{O} . To define f_i , we associate a local coordinate system with each line \mathcal{L}_i whose axis measures distance r along it from a chosen origin. Given abscissae $r_q, q \in [0, 2m_i - 1]$ of the intersections $\mathcal{S}_{i,j}$, we define the corresponding edge map as a piecewise quadratic polynomial

$$f_i(r) = \sum_{q=0}^{2m_i-2} \frac{\alpha_q(-r^2 + r(r_q + r_{q+1}) - r_q r_{q+1})}{(r_{q+1} - r_q)}, \quad (7)$$

where α_q is the positive gradient $\left| \frac{df}{dr} \right|_{r=r_q}$ defined as

$$\alpha_q = (-1)^{q+1} \alpha_0, \quad (8)$$

with α_0 being a chosen positive slope at r_0 . Fig. 5 illustrates such an edge map.

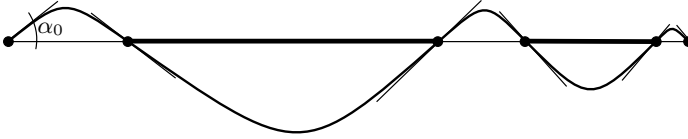


Fig. 5. Piecewise quadratic function as an edge map

4.2 Barycentric Coordinates

It is natural to consider barycentric coordinates of a polygon as homotopy variables because of the two useful properties that they offer. Barycentric coordinates span a complete polygon and are a partition of unity. Traditional barycentric coordinates for triangles (and simplices in general) are defined by its vertices. Relevant generalizations of barycentric coordinates to n -sided polygons were provided by Wachspress [16] and later by Meyer et al. [11]. In the current context, we define barycentric coordinates in terms of the edges of a polygon rather than the vertices. Such a definition allows us to apply the concepts developed so far to associate a suitable homotopy to a polygon. We define Voronoi diagram based barycentric coordinates of edges for an n -sided polygon.

An interesting class of barycentric coordinates can be derived from Voronoi diagram of line segments and a point. Consider again a polygon \mathcal{G} and a point p inside it. The Voronoi region of a point inside a polygon is a closed region of

piecewise parabolic arcs as shown in Fig. 6. From the Voronoi diagram of the edges $\{e_i\}$ in a polygon, introduction of a point p steals an area from two or more existing Voronoi regions. If the stolen area for any edge e_i and p is denoted by \mathcal{A}_i , the barycentric coordinates for the edge can be written as

$$\lambda_i = \frac{\mathcal{A}_i}{\sum_{j=0}^{s-1} \mathcal{A}_j}, i \in [0, s-1], \quad (9)$$

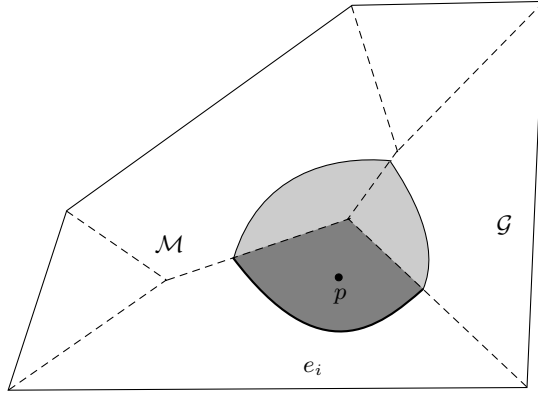


Fig. 6. Voronoi diagram of a polygon \mathcal{G} and a point p inside

Area \mathcal{A}_i can be computed as the area between the parabolic arc and the involved angle bisectors. Again, the barycentric coordinates defined in this way satisfy positivity, partition of unity and continuity. In the limiting case as p approaches one of the sides e_k , the stolen area \mathcal{A}_k becomes very small, but simultaneously areas $\mathcal{A}_{i,i \neq k}$ become smaller (and eventually zero) by a rate higher than that of the former. Thus as p approaches e_k , $\lambda_k \rightarrow 1$, and $\lambda_{i,i \neq k} \rightarrow 0$.

4.3 Homotopy

Equipped with the above defined edge maps and barycentric coordinates for any polygon \mathcal{G}_k , we define a homotopy \mathcal{H}_k in s_k variables as

$$\mathcal{H}_k(p) = \sum_{i=0}^{s_k-1} f_i(d_i(p)) \lambda_i(p), \quad (10)$$

where $d_i(p)$ is the distance along line \mathcal{L}_k from a chosen origin O_k on it until the foot of the perpendicular from point p . We can write

$$d_i(p) = \|O_k - p_i\| + (p - p_i)^T \frac{(p_{i+1} - p_i)}{l_i}, \quad (11)$$

where p_{i+1} and p_i are two end points of an edge e_i of \mathcal{G}_k lying on \mathcal{L}_k , and $\|\mathbf{x}\|$ denotes the length of a vector \mathbf{x} . Homotopy (10) continuously deforms edge maps f_i within the polygon and thus generates a smooth field. It can be seen as a linear combination of edge maps f_i with barycentric coordinates λ_i . We can further extend this so called *linear homotopy* to a *non-linear homotopy* as

$$\mathcal{H}_k(p, \eta) = \sum_{i=0}^{s_k-1} f_i(d_i(p)) \lambda_i(p)^\eta, \quad (12)$$

with η as a parameter.

Across polygons, the homotopy (10) is continuous and is at least C^1 smooth (see Appendix A for the proof). However, at all the intersection points $\mathcal{Q} = \{\mathcal{Q}_{i,j} : \mathcal{Q}_{i,j} \in \mathcal{L}_i \cap \partial\mathcal{O}\}$ of the lines $\{\mathcal{L}_i\}$ and the boundary $\partial\mathcal{O}$ of the object \mathcal{O} , the generated curve $\mathcal{H}^{-1}(0)$ is orthogonal to any line in $\{\mathcal{L}_i\}$ (see Appendix A). Therefore, the resulting reconstruction is somewhat unnatural. Given normals at the intersection points \mathcal{Q} (which is the case with many range scanning physical devices), we propose a tangent alignment scheme for the resulting curve by locally warping the domain of the homotopies.

4.4 Tangent Alignment Using Local Space Rotations

Given unit normals $\hat{\mathcal{N}}$ at intersection points \mathcal{Q} , the reconstruction can be constrained to be normally aligned to these normals at these points. We enforce this constraint by local space rotations around points \mathcal{Q} . The reconstruction

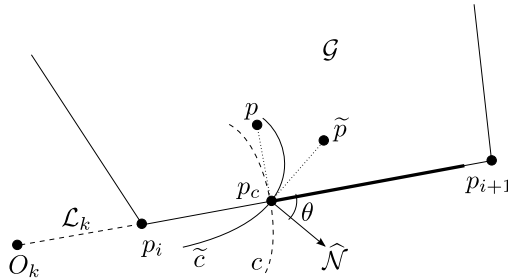


Fig. 7. Rotation of a point for tangent alignment

$c = H^{-1}(0)$ is orthogonal to the intersecting lines at \mathcal{Q} . Starting with a point p in the neighborhood of one of the points p_c of $\mathcal{Q}_{k,j}$ lying on \mathcal{L}_k , we rotate p about p_c by an angle $-\theta$ to give point \tilde{p} in the plane (see Fig. 7). The angle θ is chosen to be the signed angle between $\hat{\mathcal{N}}$ and $\nabla\mathcal{L}_k$ at the point p_c . The resulting homotopy $\tilde{\mathcal{H}}$ for a polygon \mathcal{G} can be written as

$$\tilde{\mathcal{H}} = \sum_{i=0}^{s_k-1} f_i(\tilde{d}_i) \tilde{\lambda}_i, \quad (13)$$

where,

$$\begin{aligned}\tilde{d}_i &= d_i(\tilde{p}) = \|O_k - p_i\| + (\tilde{p} - p_i)^T \frac{(p_{i+1} - p_i)}{l_i}, \text{ and} \\ \tilde{\lambda}_i &= \lambda_i(\tilde{p}) = \frac{\tilde{\mathcal{A}}_i}{\sum_{j=0}^{s-1} \tilde{\mathcal{A}}_j}, i \in [0, s-1].\end{aligned}$$

The rotated point \tilde{p} can be written as

$$\tilde{p} = p_c + \mathbf{R}(-\theta)(p - p_c), \quad (14)$$

where \mathbf{R} is the rotation matrix

$$\mathbf{R}(\theta) = \begin{bmatrix} \cos \theta & -\sin \theta \\ \sin \theta & \cos \theta \end{bmatrix}. \quad (15)$$

The modified gradient of the homotopy field in the neighborhood of p_c can be now computed using the chain rule as:

$$\nabla \tilde{\mathcal{H}} = \sum_{i=0}^{s-1} \left(f'_i(\tilde{d}_i) \nabla \tilde{d}_i \tilde{\lambda}_i + f_i(\tilde{d}_i) \nabla \tilde{\lambda}_i \right). \quad (16)$$

In the limit as point $p \rightarrow p_c$ (or the orthogonal distance to \mathcal{L}_k , $\mu_k \rightarrow 0$), using a similar derivation as given in Appendix A, we can write

$$\lim_{\mu_k \rightarrow 0} \nabla \tilde{\mathcal{H}} = f'_k(\tilde{d}_i) \nabla \tilde{d}_k \quad (17)$$

Computing the gradient of \tilde{d}_k ,

$$\begin{aligned}\nabla \tilde{d}_k &= \nabla \left((\tilde{p} - p_k)^T \frac{(p_{k+1} - p_k)}{l_k} \right) \\ &= \nabla \left((p_c + \mathbf{R}(-\theta)(p - p_c) - p_k)^T \frac{(p_{k+1} - p_k)}{l_k} \right) \\ &= \mathbf{R}(-\theta)^T \frac{(p_{k+1} - p_k)}{l_k} \\ &= \mathbf{R}(\theta) \nabla d_k\end{aligned} \quad (18)$$

Therefore,

$$\lim_{\mu_k \rightarrow 0} \nabla \tilde{\mathcal{H}} = f'_k(\tilde{d}_i) \mathbf{R}(\theta) \nabla d_k \quad (19)$$

We know that the gradient

$$\lim_{\mu_k \rightarrow 0} \nabla \mathcal{H} = f'_k(d_i) \nabla d_k. \quad (20)$$

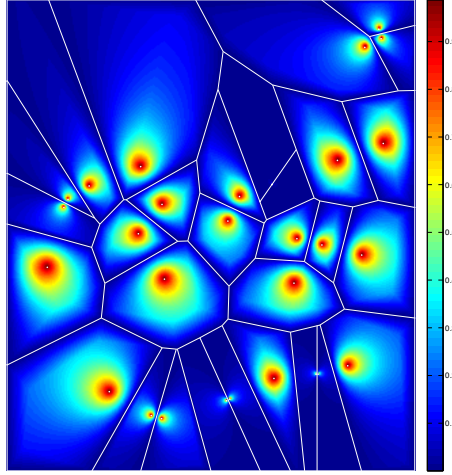


Fig. 8. Weights based on higher order Voronoi diagram

From (20) and (19) it can be seen that in the limit $\mu_k \rightarrow 0$

$$\frac{\nabla \tilde{\mathcal{H}}}{\|\nabla \tilde{\mathcal{H}}\|} = \mathbf{R}(\theta) \left(\frac{\nabla \mathcal{H}}{\|\nabla \mathcal{H}\|} \right). \quad (21)$$

Therefore, we can achieve the desired rotation of the reconstruction curve by rotating the local coordinates around the points \mathcal{Q} in the opposite direction.

4.5 Smooth Rotations of the Reconstruction Curve

In order to generate a smooth distortion $\tilde{H}^{-1}(0)$ of the curve $H^{-1}(0)$ the neighborhoods of points \mathcal{Q} must be carefully chosen. A natural neighborhood for points in \mathcal{Q} is their respective Voronoi polygons. However, a constant rotation for all the points in a particular Voronoi region results in a discontinuous curve at the boundary of these polygons. Therefore, we seek a continuous weight function w_{p_i} inside a Voronoi region $\mathcal{V}_{\mathcal{Q}}(p_i)$ of any generator $p_i \in \mathcal{Q}$ such that

$$\begin{aligned} w_{p_i}(p_i) &= 1, \text{ and} \\ w_{p_i}(\partial \mathcal{V}_{\mathcal{Q}}(p_i)) &= 0. \end{aligned} \quad (22)$$

These requirements on the weight function impose a smooth transition of rotation angles from one influence zone to another and ensure monotonically decreasing rotation angles as points get farther away from rotation centers with no rotation at the boundaries of the Voronoi regions. For any point p inside $\mathcal{V}_{\mathcal{Q}}(p_i)$, consider its nearest neighbor $p_i^{(1)}$ and the next nearest neighbor $p_i^{(2)} \in \mathcal{Q}$. Denote by $d_1(p)$ the distance between p and $p_i^{(1)}$ and by $d_2(p)$ the one between p and $p_i^{(2)}$. We can formulate the required weight function as

$$w_{p_i}(p) = \frac{d_2(p) - d_1(p)}{d_2(p) + d_1(p)}. \quad (23)$$

The first nearest neighbor $p_i^{(1)}$ is the generator point p_i of $\mathcal{V}_{\mathcal{Q}}(p_i)$. The second nearest neighbor $p_i^{(2)}$ can be found by computing the second order voronoi diagram of \mathcal{Q} . The weight function resulting from (23) is shown in Fig. 8. We outline the complete algorithm in Algorithm 1.

Input: $\{\mathcal{S}_{i,j}\}$ on $\{\mathcal{L}_i\}$, $\hat{\mathcal{N}}$ at \mathcal{Q}
Output: \mathcal{R}
 Define an edge map f_i on each \mathcal{L}_i using $\{\mathcal{S}_{i,j}\}$
 Partition \mathcal{B}_{box} into polygonal tiles $\{\mathcal{G}_k\}$ with $\{\mathcal{L}_i\}$
 Compute first order Voronoi diagram $\mathcal{V}_{\mathcal{Q}}^1$ of \mathcal{Q}
 Compute second order Voronoi diagram $\mathcal{V}_{\mathcal{Q}}^2$ of \mathcal{Q}
 Compute w from $\mathcal{V}_{\mathcal{Q}}^1$ and $\mathcal{V}_{\mathcal{Q}}^2$
for $k \in [0, p-1]$ **do**
 Compute Voronoi diagram \mathcal{V}_k of \mathcal{G}_k
 for $\mathbf{x} \in \mathcal{G}_k$ **do**
 Let $\mathbf{x}_c \in \mathcal{Q}$ be the generator of Voronoi polygon of \mathbf{x}
 $\tilde{\mathbf{x}} \leftarrow \mathbf{x}_c + \mathbf{R}(-\theta)(\mathbf{x} - \mathbf{x}_c)$
 Compute $\{\lambda_i(\tilde{\mathbf{x}})\}$ for all edges of \mathcal{G}_k using \mathcal{V}_k
 Compute $d_i(\tilde{\mathbf{x}})$ for all edges of \mathcal{G}_k
 Compute $\tilde{\mathcal{H}}_k$
 end
end
 $\tilde{\mathcal{H}} \leftarrow \bigcup \tilde{\mathcal{H}}_k$
 $\mathcal{R} \leftarrow \ker \tilde{\mathcal{H}}$

Algorithm 1. The reconstruction algorithm.

5 Results

We test our reconstruction method on a hand drawn curve intersected by a set of arbitrarily oriented lines. The lines yield a polygonal tessellation in the plane. We reconstruct the original curve from the intersections over the polygons of this tessellation.

This reconstructed curve is guaranteed to pass through the end-points of the intersections. Figs. 9(a), and 10(a) show results of our reconstruction for the linear and the non-linear homotopies respectively. The reconstructed curve is always orthogonal to the intersecting lines. The orthogonality is not apparent in Fig. 9(a) at a large scale, but is more visible for the non-linear homotopy with $\eta = 2$ in Fig. 10(a).

We also show results of the reconstructed curve after applying local rotations at points \mathcal{Q} . The local rotations distort the original curve in the desired direction as seen in Figs. 9(b), and 10(b).

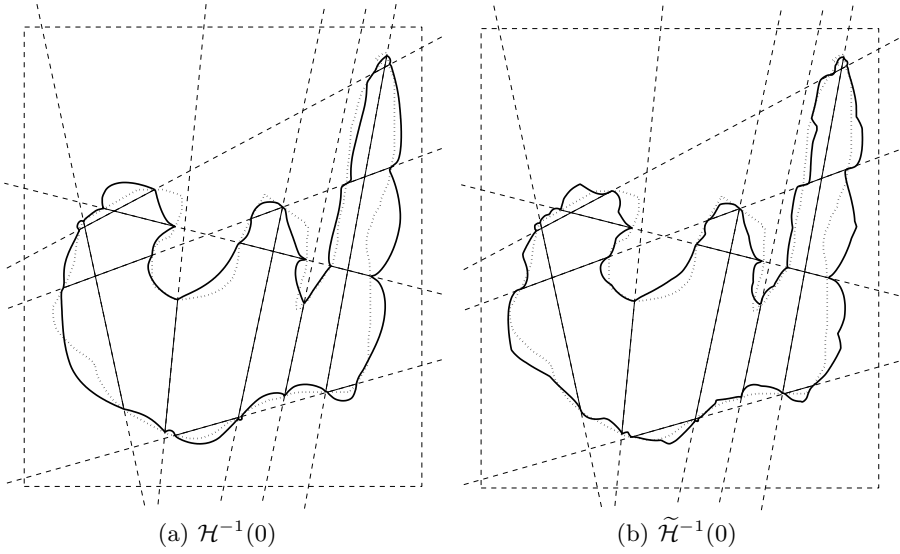


Fig. 9. Reconstruction with linear homotopy

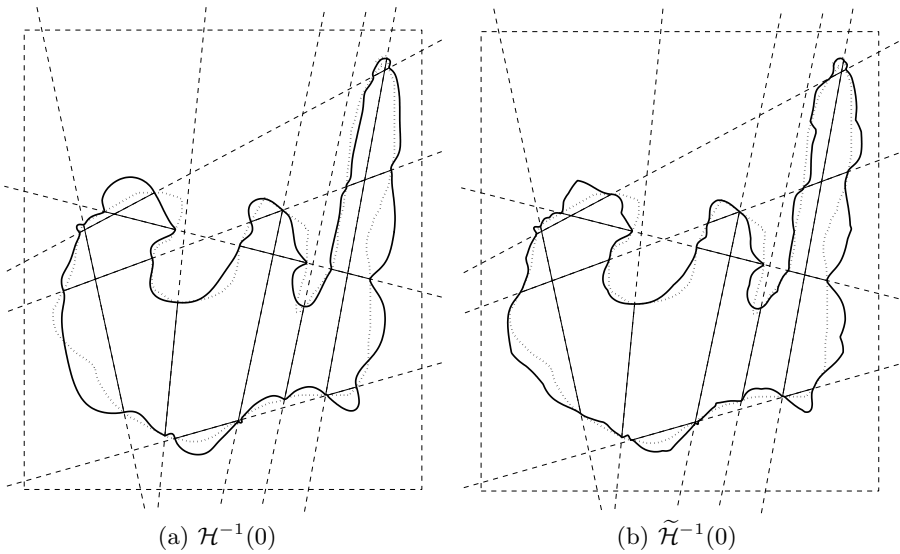


Fig. 10. Reconstruction with non-linear homotopy

The next subsection discusses accuracy statistics of our method based on how much information is provided to the reconstruction algorithm in terms of the number of intersections.

5.1 Reconstruction Accuracy

A good reconstruction depends on the choice of cutting lines placed carefully to cover salient geometric features of the object to be reconstructed. In order to test the reconstruction algorithm for accuracy, we sample intersecting lines from the skeleton of the test object. We choose to sample the skeleton of the object since it captures the salient details of the object. To show the dependence of reconstruction accuracy on the number of intersecting lines, a hierarchy of skeletons is used.

A skeleton hierarchy is computed from a straight line skeleton [2]. The hierarchy provides an incremental simplification of the skeleton based on discrete curve evolution of the skeleton branches [8,5]. Curve simplification by discrete curve evolution uses local angles at every vertex of the curve to assign a relevance to each vertex. Based on the computed relevance values, the curve is evolved (simplified) by deletion of vertices. Fig. 11 shows such a skeleton hierarchy with five levels. The base skeleton is computed using the straight line skeleton module of the CGAL library [1].

Sampled segments from the skeleton at every level are used as cutting lines for reconstruction. Thus, for every level of hierarchy of skeletons, we compute a reconstruction of the object. We next compute various error metrics for different reconstructions thus obtained. To get a comprehensive idea of the reconstruction accuracy, metrics based on area, mean distance error, and curve lengths are considered here.

Denoting the area of the model object by \mathcal{A}_{mod} , the area of the reconstruction at level i by \mathcal{A}_{rec}^i , the absolute difference of \mathcal{A}_{mod} and \mathcal{A}_{rec}^i is given by

$$\mathcal{A}_{diff}^i = \left(\mathcal{A}_{mod} \cup \mathcal{A}_{rec}^i \right) - \left(\mathcal{A}_{mod} \cap \mathcal{A}_{rec}^i \right). \quad (24)$$

Fig. 11 shows \mathcal{A}_{diff}^i for different levels of hierarchy. Another important indicator of reconstruction accuracy is the ratio of areas $\mathcal{A}_{rec}^i / \mathcal{A}_{mod}$. Both of these measures are shown in Table 1. The tests show that with better sampling, the reconstruction accuracy increases. Also the ratio of areas indicate that the reconstructed curve has a slightly larger area than the original curve.

The *Hausdorff distance* is a good measure of the distance between two manifolds [12]. Hausdorff distance, d_H , between two curves L and L' is given by

$$d_H(L, L') = \sup_{x_0 \in L} \inf_{x_1 \in L'} d(x, x'), \quad (25)$$

where $d(\cdot, \cdot)$ is an appropriate metric for measuring distance between two points in a metric space. A mean value of the Hausdorff distance can be defined as [4]

$$d_m(L, L') = \frac{1}{|L|} \int_{x \in L} \inf_{x' \in L'} d(x, x') dL, \quad (26)$$

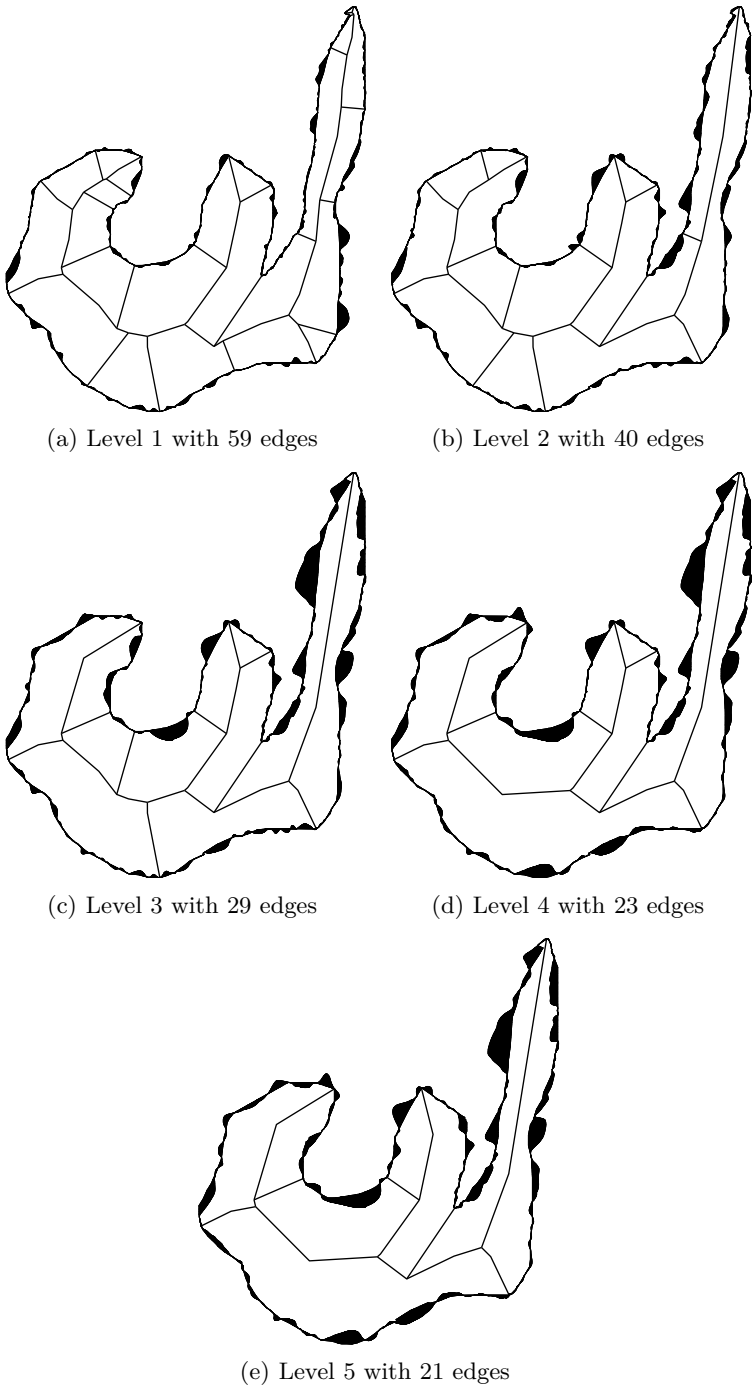


Fig. 11. Skeleton hierarchy and reconstruction accuracy

Table 1. Reconstruction accuracy with respect to areas

		$\mathcal{A}_{mod} = 0.3228$			
Level	Edges	\mathcal{A}_{rec}^i	\mathcal{A}_{diff}^i	$\% \left(\frac{\mathcal{A}_{diff}^i}{\mathcal{A}_{mod}} \right)$	$\frac{\mathcal{A}_{rec}^i}{\mathcal{A}_{mod}}$
1	59	0.3266	0.0123	3.8	1.0119
2	40	0.3247	0.0168	5.2	1.0058
3	29	0.3279	0.0297	9.2	1.0160
4	23	0.3287	0.0333	10.3	1.0182
5	21	0.3283	0.0349	10.8	1.0171

where $|L|$ is the length of the curve L . A relative value of this distance is computed with respect to the bounding box of the object, as shown in Table 2. Also shown in the table is the length ratio of the reconstructed curve with respect to the original object contour. Here again, the tests show that a better sampling increases the accuracy of the reconstruction. However, we must point out that a topologically correct reconstruction is achievable with as few cutting lines as there are salient features in the object.

Table 2. Reconstruction accuracy with respect to lengths

Level Edges		$\% \left(\frac{d_H}{L_{diag}} \right)$	$\frac{L_{rec}}{L_{mod}}$
1	59	0.75	1.0842
2	40	0.82	1.0919
3	29	1.02	1.1227
4	23	1.08	1.1191
5	21	1.11	1.1186

5.2 Comparison

A comparison of our reconstruction with the results of Memari and Boissonnat [10] shows some of the shortcomings of their method that can be overcome with a reconstruction using continuous deformations. Reconstruction method proposed by Memari and Boissonnat is derived from the Delaunay complex of the cross sections. The reconstruction curve (see Fig. 12) is only C^0 and misses some of the high curvature regions of the original object boundary.

We produce comparative statistics for our reconstruction with the method by Memari and Boissonnat [10]. The measures used for comparison are based on area and length of the reconstructed curve as introduced in the previous subsection. Table 3 shows reconstruction accuracy of three methods for the set of intersection lines shown in Fig. 4. Here, Homotopy₁ refers to the reconstruction using continuous deformations with no tangent alignment and Homotopy₂ refers to the reconstruction resulting from tangent alignment. Since [10] results in a

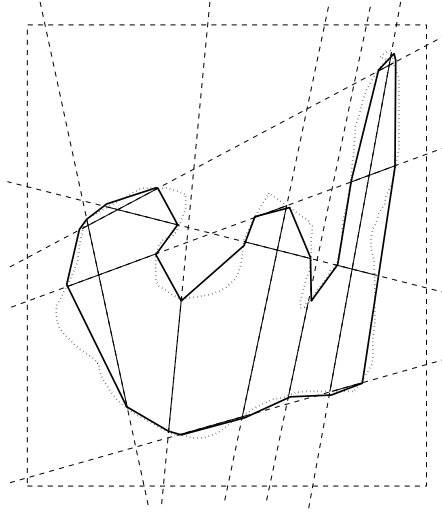


Fig. 12. Piecewise linear reconstruction using algorithm by Memari and Boissonnat [10]

piecewise linear reconstruction, the area (possibly) and length of the curve are underestimated. The ratio of absolute difference of area with the area of the model is low for Memari’s reconstruction that matches up with Homotopy₂ reconstruction, but the relative Hausdorff measure goes bad and turns out to be more than double of that obtained with either of the Homotopy based reconstructions. Further, the relative ratio of the lengths of the reconstruction and the original object shows that homotopy based reconstructions perform better with estimating the length of the object.

Table 3. Comparison of Reconstructions

Method	$\% \left(\frac{\mathcal{A}_{diff}}{\mathcal{A}_{mod}} \right)$	$\frac{\mathcal{A}_{rec}}{\mathcal{A}_{mod}}$	$\% \left(\frac{d_H}{L_{diag}} \right)$	$\frac{L_{rec}}{L_{mod}}$
Memari [10]	14.6025	0.9652	3.9323	0.9149
Homotopy ₁	17.5470	1.0407	1.4831	1.0256
Homotopy ₂	14.6690	1.0425	1.3243	1.0303

6 Conclusion

In this work, we have presented a novel method of curve reconstruction from arbitrary cross sections in a planar setting. The presented algorithm uses continuous deformations to reconstruct the object smoothly. We also introduced generalized barycentric coordinates for polygons defined on its edges using the line and point Voronoi diagram. The presented method is general in nature and

can be applied to higher dimensions. We evaluate accuracy of our algorithm based on sampling of the original object.

An interesting generalization of the problem of reconstruction from arbitrary cross sections is 3D reconstruction from arbitrary cutting planes. These cutting planes partition the domain of computation into polyhedra, and also embed the intersection with the object. Similar to the approach suggested in this paper, a function $f : \mathbb{R}^2 \mapsto \mathbb{R}$ can be embedded in a cutting plane such that $\ker(f)$ represents the boundary of this intersection. An example of one such function is the signed distance function. Higher degree polynomial functions can be designed based on this distance function. A multi-variate homotopy can then be constructed from the functions defined previously on the faces of a polyhedron. A possible parameterization of such a homotopy is with respect to the orthogonal distance of any point inside the polyhedron to the polyhedron faces (see Figure 13). Parameterization in terms of the Voronoi volume (a volume consisting of a paraboloid face and planar faces) stolen by a point inside the polyhedron is another choice. A union of the zero level set of the derived homotopies provides a reconstruction surface.

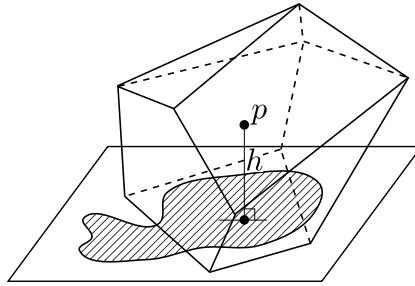


Fig. 13. Reconstruction from arbitrary cutting planes in \mathbb{R}^3 . The polyhedron shows one of the partitions of the domain resulting from cutting planes (one such shown here). The shaded region depicts the cross section of the 3D object with the cutting plane.

Appendix A: Smoothness in Homotopies

Proposition 1. *For a triangle \mathcal{T} in a planar triangulation, we show that the curve $\mathcal{H}^{-1}(0)$ defined by the homotopy (10),*

$$\mathcal{H}(p) = \sum_{i=0}^2 f_i(d_i(p)) \lambda_i(p) = 0,$$

is at least C^1 .

Proof. We can prove this by showing that $\mathcal{H}^{-1}(0)$ is C^0 and C^1 .

1. $\mathcal{H}^{-1}(0)$ is C^0 .

From the properties of barycentric coordinates, we know that

$$\sum_{i=0}^2 \lambda_i = 1.$$

This implies that at any edge e_k of \mathcal{T} , $\lambda_k = 1$ and $\lambda_{i,i \neq k} = 0$. Therefore, for any p lying on e_k , $\mathcal{H}(p) = f_k(d_k(p))$. The same holds for any other triangle in the triangulation and since the functions f_i are globally defined on lines L_i , $\mathcal{H} = 0$ is C^0 .

2. $\mathcal{H}^{-1}(0)$ is C^1 .

In order to show that $\mathcal{H}^{-1}(0)$ is C^1 , we calculate the gradient of \mathcal{H} at any e_k . The derivative of \mathcal{H} is

$$\nabla \mathcal{H} = \sum_{i=0}^2 (f'_i(d_i) \nabla d_i \lambda_i + f_i(d_i) \nabla \lambda_i) \quad (27)$$

where d_i is the distance along line \mathcal{L}_j corresponding to edge e_i of the triangle. For a triangle, the proposed barycentric coordinates based on the stolen area \mathcal{A}_i for any edge e_i and point p are given by (9) as

$$\lambda_i = \frac{\mathcal{A}_i}{\sum_{j=0}^2 \mathcal{A}_j}, i \in [0, 2].$$

The gradient of λ_i can be calculated using the chain rule as

$$\begin{aligned} \nabla \lambda_i &= \frac{\frac{\nabla \mathcal{A}_i}{2}}{\sum_{j=0}^2 \mathcal{A}_j} - \frac{\mathcal{A}_i}{\left(\sum_{j=0}^2 \mathcal{A}_j\right)^2} \sum_{j=0}^2 \nabla \mathcal{A}_j \\ &= \frac{\frac{\nabla \mathcal{A}_i}{2}}{\sum_{j=0}^2 \mathcal{A}_j} - \lambda_i \sum_{j=0}^2 \frac{\frac{\nabla \mathcal{A}_j}{2}}{\sum_{j=0}^2 \mathcal{A}_j} \end{aligned} \quad (28)$$

Using (27) and (28),

$$\nabla \mathcal{H} = \sum_{i=0}^2 \left(f'_i(d_i) \nabla d_i \lambda_i + f_i(d_i) \left[\frac{\frac{\nabla \mathcal{A}_i}{2}}{\sum_{j=0}^2 \mathcal{A}_j} - \lambda_i \sum_{j=0}^2 \frac{\frac{\nabla \mathcal{A}_j}{2}}{\sum_{j=0}^2 \mathcal{A}_j} \right] \right) \quad (29)$$

To compute the gradient of \mathcal{H} at the intersection of line \mathcal{L}_j and the object, we must take the derivative at a point p in the limit as p approaches line \mathcal{L}_j . In this limit,

$$\begin{aligned}\lambda_k &\rightarrow 1 \\ \lambda_{i,i \neq k} &\rightarrow 0\end{aligned}\tag{30}$$

Before the gradient in the limit can be evaluated, the behavior of $\nabla \mathcal{A}_i$ and \mathcal{A}_i should be analyzed. To do so, we define several quantities as following.

Consider the triangle \mathcal{T} shown in Fig. 14. Let the vertices of \mathcal{T} be denoted by $p_0(x_0, y_0)$, $p_1(x_1, y_1)$, and $p_2(x_2, y_2)$, and the edges by $e_0 = (p_1 - p_0)$, $e_1 = (p_2 - p_1)$, and $e_2 = (p_0 - p_2)$. Let an edge e_i of \mathcal{T} be parameterized by distance α along it

$$e_i : p = p_i + \alpha \frac{(p_{i+1} - p_i)}{l_i}, \quad (31)$$

where index i is to be taken in a circular sense in the triangle. The Voronoi diagram of edges of \mathcal{T} divide it internally in three regions. We consider a point p lying in the Voronoi region of an edge e_i of \mathcal{T} (see Fig. 14).

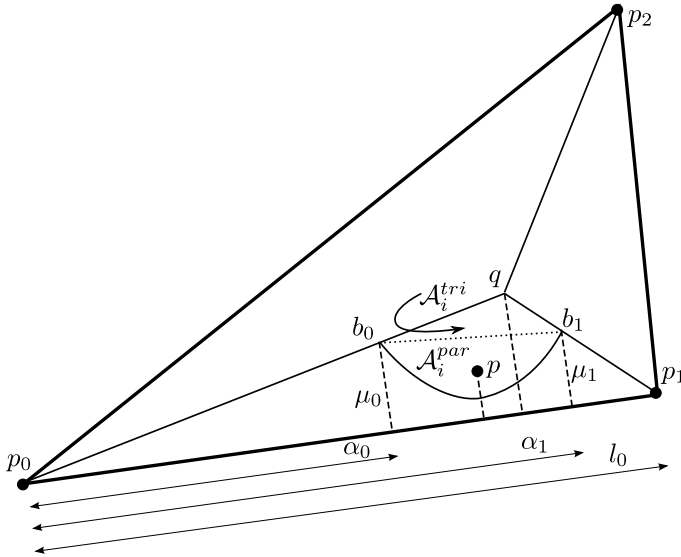


Fig. 14. Parameterization along triangle edge

A parabola with focus at point p and directrix e_i is given by

$$\mathcal{P}_i : \mu(\alpha) = \frac{(\alpha - \alpha_p)^2}{2\mu_p} + \frac{\mu_p}{2}, \quad (32)$$

where (α, μ) form an orthonormal basis, and

$$\alpha_p = (p - p_i)^T \frac{(p_{i+1} - p_i)}{l_i}, \quad (33)$$

$$\mu_p = (p - p_i)^T \mathbf{M} \frac{(p_{i+1} - p_i)^T}{l_i}, \quad (34)$$

with

$$\mathbf{M} = \begin{bmatrix} 0 & 1 \\ -1 & 0 \end{bmatrix}, \quad (35)$$

and l_i is the length of e_i .

Let the parabola \mathcal{P}_i intersects the boundary of the Voronoi region at points $b_i(\alpha_0, \mu_0)$ and $b_{i+1}(\alpha_1, \mu_1)$ respectively. Denote by $q(\alpha_q, \mu_q)$ the incenter of \mathcal{T} . The parabola can intersect the two angle bisectors of the triangle $\mathcal{B}_i : \mu = k_0\alpha$, and $\mathcal{B}_{i+1} : \mu = k_1(l_i - \alpha)$, $k_i = \tan(\theta_i/2)$, in three possible ways

- I. $\alpha_1 \leq \alpha_q$: both branches of the parabola intersect \mathcal{B}_i , and $\mu_m = k_0\alpha_m$, $m = \{0, 1\}$,
- II. $\alpha_0 \geq \alpha_q$: both branches of the parabola intersect \mathcal{B}_{i+1} , and $\mu_m = k_1(l_i - \alpha_m)$, $m = \{0, 1\}$, and
- III. $\alpha_0 < \alpha_q$ and $\alpha_1 > \alpha_q$: the branches of the parabola intersect \mathcal{B}_i and \mathcal{B}_{i+1} respectively, and $\mu_0 = k_0\alpha_0$ and $\mu_1 = k_1(l_i - \alpha_1)$.

It is sufficient to treat one of these cases here. Considering case I, α_0 and α_1 are the roots of

$$\alpha^2 - 2\alpha(\alpha_p + k_0\mu_p) + (\alpha_p^2 + \mu_p^2) = 0. \quad (36)$$

The areas to compute the barycentric coordinates can be written as

$$\mathcal{A}_i = \mathcal{A}_i^{par} + \mathcal{A}_i^{tri} \quad (37)$$

where, \mathcal{A}_i^{par} is the area enclosed between the parabolic arc and line connecting b_i and b_{i+1} , and \mathcal{A}_i^{tri} is the area of the triangle connecting points b_i , b_{i+1} , and q . Using (32)

$$\mathcal{A}_i^{par} = \frac{\mu_0 + \mu_1}{2}(\alpha_1 - \alpha_0) - \int_{\alpha_0}^{\alpha_1} \left(\frac{(\alpha - \alpha_p)^2}{2\mu_p} + \frac{\mu_p}{2} \right) d\alpha, \quad (38)$$

and

$$\mathcal{A}_i^{tri} = \frac{\mu_0 + \mu_q}{2}(\alpha_q - \alpha_0) + \frac{\mu_1 + \mu_q}{2}(\alpha_1 - \alpha_q) - \frac{\mu_0 + \mu_1}{2}(\alpha_1 - \alpha_0). \quad (39)$$

Therefore,

$$\mathcal{A}_i = \frac{\mu_0 + \mu_q}{2}(\alpha_q - \alpha_0) + \frac{\mu_1 + \mu_q}{2}(\alpha_1 - \alpha_q) - \int_{\alpha_0}^{\alpha_1} \left(\frac{(\alpha - \alpha_p)^2}{2\mu_p} + \frac{\mu_p}{2} \right) d\alpha \quad (40)$$

Note that (40) holds for all the three cases above. Simplifying (40), we get

$$\begin{aligned}
2\mathcal{A}_i &= (\mu_0 + \mu_q)(\alpha_q - \alpha_0) + (\mu_1 + \mu_q)(\alpha_1 - \alpha_q) - \left[\frac{(\alpha - \alpha_p)^3}{3\mu_p} - \mu_p \alpha \right]_{\alpha_0}^{\alpha_1} \\
&= (\mu_0 + \mu_q)(\alpha_q - \alpha_0) + (\mu_1 + \mu_q)(\alpha_1 - \alpha_q) \\
&\quad - \frac{(\alpha_1 - \alpha_p)^3 - (\alpha_0 - \alpha_p)^3}{3\mu_p} - \mu_p(\alpha_1 - \alpha_0)
\end{aligned} \tag{41}$$

Distance d_i in (10) can be written as

$$d_i(p) = \|O_j - p_i\| + \alpha_p, \tag{42}$$

where we know that p_i lies on \mathcal{L}_j and O_j is the chosen origin on \mathcal{L}_j . We note the following derivatives

$$\begin{aligned}
2\nabla\mathcal{A}_i &= \nabla\alpha_0(-\mu_0 - \mu_p) + \nabla\alpha_1(\mu_1 + \mu_p) + \nabla\mu_0(-\alpha_0 + \alpha_q) + \nabla\mu_1(\alpha_1 - \alpha_q) \\
&\quad + \frac{(\alpha_1 - \alpha_p)^3 - (\alpha_0 - \alpha_p)^3}{3\mu_p^2} \nabla\mu_p - \frac{(\alpha_1 - \alpha_p)^2(\nabla\alpha_1 - \nabla\alpha_p)}{\mu_p} \\
&\quad + \frac{(\alpha_0 - \alpha_p)^2(\nabla\alpha_0 - \nabla\alpha_p)}{\mu_p} - (\alpha_1 - \alpha_0)\nabla\mu_p - \mu_p(\nabla\alpha_1 - \nabla\alpha_0)
\end{aligned} \tag{43}$$

$$\nabla d_i = \nabla\alpha_p = \frac{(p_{i+1} - p_i)}{l_i} \tag{44}$$

$$\nabla\mu_p = \mathbf{M} \frac{(p_{i+1} - p_i)}{l_i} \tag{45}$$

$$\nabla\alpha_m = \frac{\nabla\alpha_p(\alpha_m - \alpha_p) + \nabla\mu_p(\mu_m - \mu_p)}{(\alpha_m - \alpha_p - k_0\mu_p)}, m = \{0, 1\} \tag{46}$$

$$\nabla\mu_m = k_0\nabla\alpha_m, m = \{0, 1\} \tag{47}$$

In the limit $\mu_p \rightarrow 0$ for some edge e_k of \mathcal{T} ,

$$\begin{aligned}
\alpha_m &\rightarrow \alpha_p, m \in \{0, 1\} \\
\mu_m &\rightarrow k_0\alpha_p, m \in \{0, 1\}
\end{aligned} \tag{48}$$

Consequently, $\mathcal{A}_i \rightarrow 0$, but $\mathcal{A}_{i,i \neq k}$ becomes 0 much faster than \mathcal{A}_k . Therefore, using (30) and (48), the gradient (29) in the limit is

$$\begin{aligned}
\lim_{\mu_p \rightarrow 0} \nabla\mathcal{H} &= f'_k(d_k)\nabla d_k + f_k(d_k) \left[\frac{\frac{\nabla\mathcal{A}_k}{2}}{\sum_{j=0} \mathcal{A}_j} - \frac{\frac{\nabla\mathcal{A}_k}{2}}{\sum_{j=0} \mathcal{A}_j} \right] \\
&= f'_k(d_k)\nabla d_k.
\end{aligned} \tag{49}$$

Gradient of line e_k is

$$\nabla e_k = \mathbf{M} \frac{(p_{i+1} - p_i)}{l_i}. \tag{50}$$

We note that

$$\begin{aligned} \left\langle \lim_{\mu_p \rightarrow 0} \nabla \mathcal{H}, \nabla e_k \right\rangle &= f'_k(d_k) \frac{(p_{i+1} - p_i)^T}{l_i} \mathbf{M} \frac{(p_{i+1} - p_i)}{l_i} \\ &= 0. \end{aligned}$$

A similar result can be shown for the gradient of the homotopy on the other side of \mathcal{L}_j . This implies that the reconstructed curve is orthogonal to the intersecting lines from either side.

Therefore, the curve reconstruction is at least C^1 . \square

References

1. CGAL, Computational Geometry Algorithms Library, <http://www.cgal.org>
2. Aichholzer, O., Aurenhammer, F., Alberts, D., Gärtner, B.: A novel type of skeleton for polygons. *Journal of Universal Computer Science* 1(12), 752–761 (1995)
3. Allgower, E.L., Georg, K.: *Numerical continuation methods: an introduction*. Springer-Verlag New York, Inc., New York (1990)
4. Aspert, N., Santa-Cruz, D., Ebrahimi, T.: Mesh: Measuring errors between surfaces using the hausdorff distance. In: *Proceedings of the IEEE International Conference on Multimedia and Expo.*, vol. 1, pp. 705–708 (2002)
5. Bai, X., Latecki, L., Liu, W.: Skeleton pruning by contour partitioning with discrete curve evolution. *IEEE Transactions on Pattern Analysis and Machine Intelligence* 29(3), 449–462 (2007)
6. Dougherty, G., Varro, J.: A quantitative index for the measurement of the tortuosity of blood vessels. *Medical Engineering & Physics* 22(8), 567–574 (2000)
7. Jänich, K.: *Topology*, Undergraduate texts in mathematics (1984)
8. Latecki, L.J., Lakämper, R.: Polygon Evolution by Vertex Deletion. In: Nielsen, M., Johansen, P., Fogh Olsen, O., Weickert, J. (eds.) *Scale-Space 1999*. LNCS, vol. 1682, pp. 398–409. Springer, Heidelberg (1999)
9. Liu, L., Bajaj, C., Deasy, J.O., Low, D.A., Ju, T.: Surface reconstruction from non-parallel curve networks. *Computer Graphics Forum* 27, 155 (2008)
10. Memari, P., Boissonnat, J.D.: Provably Good 2D Shape Reconstruction from Unorganized Cross-Sections. *Computer Graphics Forum* 27, 1403–1410 (2008)
11. Meyer, M., Lee, H., Barr, A., Desbrun, M.: Generalized barycentric coordinates on irregular polygons. *Journal of Graphics, GPU, and Game Tools* 7(1), 13–22 (2002)
12. Munkres, J.: *Topology*, 2nd edn. Prentice Hall (1999)
13. Patasius, M., Marozas, V., Lukosevicius, A., Jegelevicius, D.: Model based investigation of retinal vessel tortuosity as a function of blood pressure: preliminary results. In: *29th Annual International Conference of the IEEE Engineering in Medicine and Biology Society*, pp. 6459–6462 (2007)
14. Saucan, E., Appleboim, E., Zeevi, Y.Y.: Geometric approach to sampling and communication. *Arxiv preprint arXiv:1002.2959* (2010)
15. Sidlesky, A., Barequet, G., Gotsman, C.: Polygon Reconstruction from Line Cross-Sections. In: *Canadian Conference on Computational Geometry* (2006)
16. Wachspress, E.L.: *A rational finite element basis*. Academic Press (1975)